PHYSICAL REVIEW FLUIDS **1**, 073902 (2016)

Wenzel to Cassie transition during droplet impingement on a superhydrophobic surface

Cristian E. Clavijo,[*] Julie Crockett, and Daniel Maynes
Brigham Young University, Provo, Utah 84602, USA

(Received 5 February 2016; published 4 November 2016)

Superhydrophobic surfaces offer many industrial advantages such as drag reduction and self-cleaning behavior as long as the liquid remains suspended above the composite solid/gas interface (Cassie state). These advantages are hindered when liquid penetrates the gas cavities (Wenzel state), and this is commonly referred to as impalement. Current efforts to drive impaled liquid out of, or dewet, the cavities—such as boiling or mechanical vibrations—are locally disruptive to the flow. In this work, we reveal that passive dewetting is possible during droplet impingement on micropillar substrates under the right thermodynamical conditions. Exploration included substrates with pillar-to-pillar spacing of 8 and 16 μm, pillar diameters of 3 and 6 μm, and pillar heights of 4 to 8 μm and 8 to 18 μm, respectively. The substrate temperature range considered was $23 < T_s < 96\,^{\circ}$C. Results revealed that dewetting increases with increasing pillar height and increasing substrate temperature. Two hypotheses for the driving mechanism are formulated based on evaporation and surface energy. First-order models are consequently constructed, revealing that dewetting does not occur due to evaporation, but is caused by surface energy gradients at the interface. Dissipation in the flow is taken into account due to hydrodynamic and nonhydrodynamic mechanisms; the latter is found to dominate resistance.

DOI: 10.1103/PhysRevFluids.1.073902

I. INTRODUCTION

The behavior of a liquid that comes in contact with a solid surface is highly influenced by the wettability of the surface [1–3]. One commonly used metric to macroscopically determine the extent of hydrophobicity is the static contact angle formed at the triple contact line, which for water is generally between 90° and 120° on a hydrophobic solid [4]. If the hydrophobic substrate exhibits nano- or microscale roughness, however, contact angles can exceed 150°, and such substrates are referred to as superhydrophobic (SH) [4–6]. Surface roughness allows many types of plants [7] and insects [8,9] to thrive in nature and enables unique characteristics that promote extremely low adhesion to water solutions [10]. Consequently, drag-reduction [11–14], self-cleaning [15], and enhanced drop-wise condensation [16] surfaces can be realized. These characteristics are made possible by the existence of a solid/gas composite layer at the interface (Cassie state). Superhydrophobic substrates are finding use in many man-made applications, ranging from medicine to microelectronics [3], and are also of great fundamental interest [17–22].

If liquid impregnates the cavities (Wenzel state), hereafter referred to as impalement, many of the advantages posed by the superhydrophobic effect are compromised due to the dramatic increase in apparent adhesion between liquid and solid. It is, therefore, of significant interest to understand the thermodynamic landscape between the Cassie and Wenzel states in order to avoid transition from the former to the latter or to investigate possible pathways of reversibility once impalement has occurred. The transition between these two potential energy minima [23] has indeed been under great recent scrutiny [23–33].

Whether a sessile droplet resides in the Cassie or Wenzel state depends on the architecture of the SH substrate. For instance, the pressure difference, ΔP, required for impalement on a pattern

---

[*] Corresponding author: cristian@byu.edu

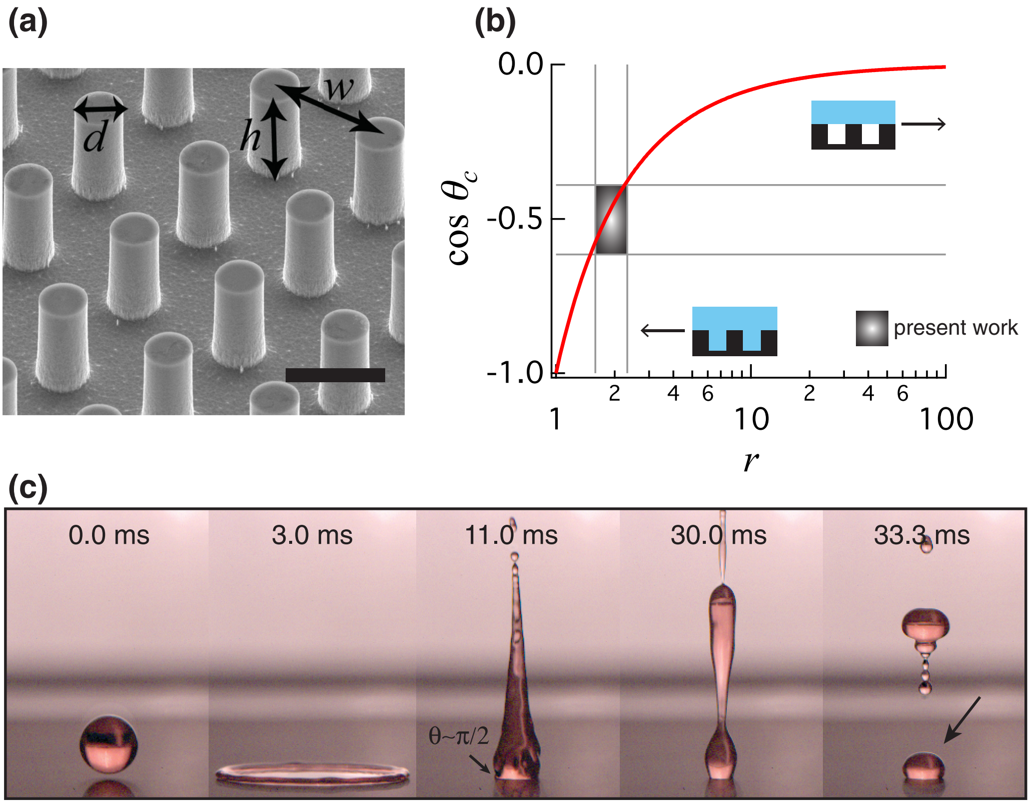

FIG. 1. (a) SEM photograph of superhydrophobic substrate used in this work. (b) $\cos\theta_c$ is plotted as a function of r for $\phi_s = 0.2$, where the Cassie or Wenzel state becomes more energetically favorable for $r \to \infty$ and $r \to 1$, respectively. (c) A 3 mm diameter water droplet impacting a superhydrophobic substrate: ($t = 0.0$ ms) prior to impact; ($t = 3.0$ ms) maximum spread; ($t = 11.0$ ms) apparent contact angle at the interface is no longer in the superhydrophobic regime, $\theta \sim \pi/2$; ($t = 30.0$ ms) necking between the rebounding and the pinned liquid becomes evident; ($t = 33.3$ ms) droplet separation has occurred and pinned liquid remains behind in the Wenzel state as indicated by the arrow.

of alternating rectangular ribs and cavities decreases with increasing cavity length, l, as $\Delta P \sim l^{-1}$ and thus the likelihood of impalement increases with cavity size [24]. Other factors that play a role include the solid fraction, ϕ_s, defined as the solid area in contact with the liquid divided by the projected area; Young, or static, contact angle, θ_e; and roughness factor, r, defined as the total solid surface area divided by the projected area, which for a pillar-type arrangement depicted in Fig. 1(a) is $r = 1 + \pi dh/w^2$ (d is the pillar diameter, h is the pillar height, and w is the pillar center-to-center spacing or pitch). The concept of a critical contact angle, θ_c, was defined by Bico *et al.* [34] as $\cos\theta_c = (\phi_s - 1)/(r - \phi_s)$ and is plotted in Fig. 1(b) as a function of r for $\phi_s = 0.2$, which is a typical solid fraction. If $\cos\theta_e$ is larger than $\cos\theta_c$, then the Wenzel state is highly favored and becomes increasingly more so as $r \to 1$. On the other hand, if $\cos\theta_e$ is smaller than $\cos\theta_c$, energetic favorability is given to the Cassie state.

For a Cassie droplet on a substrate with moderate r values, the Cassie state is generally said to be metastable and becomes vulnerable to impalement for bouncing droplets due to local pressure increase [35,36]. Figure 1(c) depicts a millimetric droplet bouncing on a SH substrate for a pillar structured surface ($w = 16$ μm and $h = 18$ μm). Here, impalement occurs at impact and, as the droplet rebounds, the impaled liquid leaves a smaller drop behind (time $t \sim 33.3$ ms). These images illustrate the general frailty of a microstructured SH substrate where, if several droplets continuously impact it, the substrate may not remain "dry." Cassie stability can be enhanced by employing hierarchical substrates such as nanoscale roughness on microfeatures [36,37] or simply very tall microfeatures [35], either of which effectively increases r by increasing the total solid surface area. However, moderate microstructured SH substrates (smallest feature size $\sim 10^0$–10^2 μm) are often desired in droplet-impingement applications due to the associated large hydrodynamic [6,38] and/or thermal [39] slip effects. Thus, it has become of interest to investigate impalement reversibility pathways for micro-structured substrates, which thus far has proven difficult [25,40,41]. We address this issue in the present work.

Impalement into a SH micropillar substrate during droplet impingement was reported by Reyssat *et al.* [35]. The pillars were 2.5 and 10 μm in diameter and height, respectively. Though impingement was axisymmetric, the impaled region exhibited sharp corners due to the lattice arrangement of the pillars, which coincide with the arrangement used in this work. Later, Krupenkin *et al.* investigated Wenzel to Cassie dynamics for a sessile ionic water droplet on micropillar SH substrates with lattice arrangement similar to that of Reyssat *et al.* [35], which was induced into the Wenzel state by applying voltage between the droplet and substrate [26,41]. The temperature at the solid-liquid interface (originally at room temperature) was increased instantaneously well above saturation temperature ($>200\,^\circ$C) by running a current through a thin conductive layer coated on the surface. This caused the liquid at the interface to vaporize and thus the droplet rapidly ($\sim$50 ms) returned to the Cassie state. While this technique achieves a Wenzel to Cassie transition, the mechanisms used may be adverse in applications where high temperatures are detrimental. Similar approaches have been attempted by other groups [42], as well as magnetism [43], electrolysis [44], vibrations [16], and more recently, hemiwicking of a low surface tension liquid [45]. However, there are no current solutions for passive transition back to the Cassie state once liquid has impaled the surface. In this paper, we discuss a mechanism through which this transition occurs during droplet impingement, which we shall refer to as "dewetting." Specifically, we explore millimetric water droplet impingement on SH substrates composed of micropillar structures [Fig. 1(a)]. The influences of substrate temperature (below saturation temperature of water), pillar height, and pitch are quantified.

In Sec. II experimental and data processing methodologies are detailed. Experimental results showing the influence of substrate temperature, micro-structure height and spacing on dewetting are discussed in Sec. III. In Section IV, first-order models are postulated to explain the behavior and identify the mechanisms at play. Although not the primary point of the paper, the mathematical development of the observations reveal that the experiments lend themselves to the isolation of contact line dissipation from hydrodynamic dissipation, which is difficult to achieve experimentally [46]. Finally, the results are summarized and conclusions drawn in Sec. V.

II. METHODOLOGY

Superhydrophobic substrates arrayed with micropillars [SEM photograph shown in Fig. 1(a)] were fabricated on 4-inch silicon wafers ($\sim$500 μm thick) using photolithography and reactive-ion etching. Once etched to the desired depth, the substrates were coated with a $\sim$100 nm chromium layer in an electron beam evaporator to promote adhesion of a subsequent $\sim$200 nm thick layer fluoropolymer [4,5-difluoro-2,2-bis(trifluoromethyl)-1,3-dioxole].

Seven different substrate geometries were created with constant solid fraction, $\phi_s \sim 0.11$, but varying pitch and height. Three substrates exhibited an 8 μm pitch, nominal pillar diameters of 3 μm, and 4, 6, and 8 μm pillar heights. The other four substrates exhibited a 16 μm pitch, nominal pillar diameter of 6 μm, and 8, 12, 16, and 18 μm pillar heights. These geometrical parameters were chosen such that water would reach the bottom of the cavities during impalement, thus pinning the rebound [47]. Reyssat *et al.* [35] showed that impalement does not fully penetrate for $h/(w-d)^2 > 10^6$ m^{-1} for a water droplet impinging at a velocity similar to those investigated here. For the tallest pillars in both the 8 and 16 μm pitch substrates, $h/(w-d)^2 = 0.32 \times 10^6$ and 0.18×10^6 m^{-1}, respectively, thus showing we are well within the complete impalement threshold.

TABLE I. Average values of profilometer measurements of pillar-arrayed superhydrophobic substrates. Values for w, h, and d are given in μm, while ϕ_s and r are dimensionless.

w/h	d	ϕ_s	r	w/h	d	ϕ_s	r
8/4	3.0	0.11	1.59	16/8	6.0	0.11	1.59
8/6	3.1	0.11	1.88	16/12	6.4	0.13	1.96
8/8	2.8	0.10	2.12	16/16	5.9	0.11	2.18
				16/18	6.1	0.11	2.32

This will also be evidenced by the experimental results presented later. From here on, we will refer to the substrates by the following convention: XpYh (e.g., 8p6h refers to the 8 μm pillar pitch, 6 μm pillar height substrate). Pillar height variation across a single substrate (within the region of interest) was on the order of 2%. Final values of pillar diameters, d, and resultant ϕ_s and r are reported in Table I. The apparent static contact angle, θ, for a sessile water droplet in the Cassie state for all substrates was nominally $166 \pm 3^\circ$ with a hysteresis of $\sim 20^\circ$.

Experiments were conducted by releasing a single water droplet from 20 cm above a horizontally positioned SH substrate as shown in Fig. 2. One droplet size ($\sim$24 μl) and impact velocity, V_o ($\sim$1.96 m/s), were considered across all tests. These were chosen such that the droplet would spread out sufficiently far during impingement and allow a clear view of the impaled region. The resulting impact Weber number, $\mathrm{We}_o = \rho_o V_o^2 D_o/\sigma_o$, was nominally 190 ($\rho$ is liquid density, D is droplet diameter, σ is liquid-gas surface tension, and the subscript o is used to denote preimpact conditions at room temperature). D_o was obtained with a high speed camera positioned parallel to the substrate and V_o by fitting a curve to the temporal position of the falling droplet. Uncertainty in V_o and D_o was approximately 1%, while uncertainties in the fluid properties ρ_o and σ_o were 0.2% and 0.7%. Overall uncertainty in We_o was 3.7%.

The superhydrophobic substrate was placed on top of an aluminum block which was heated from the bottom with the sides insulated. Four type-K thermocouples (error for absolute measurement $\sim$2.2 °C) were embedded 1 mm below the top of the block at different locations, revealing that the temperature variation across that plane of the block was less than 1 °C. To determine substrate

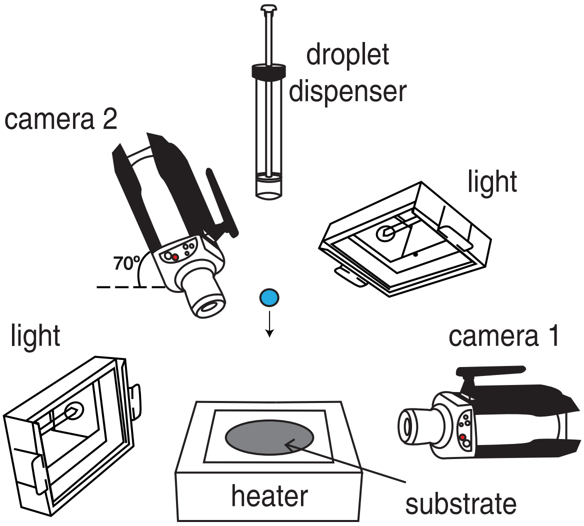

FIG. 2. Schematic of the experimental setup illustrating the position of the substrate on the heater block and high-speed cameras 1 and 2, which captured droplet impact velocity and dewetting dynamics, respectively.

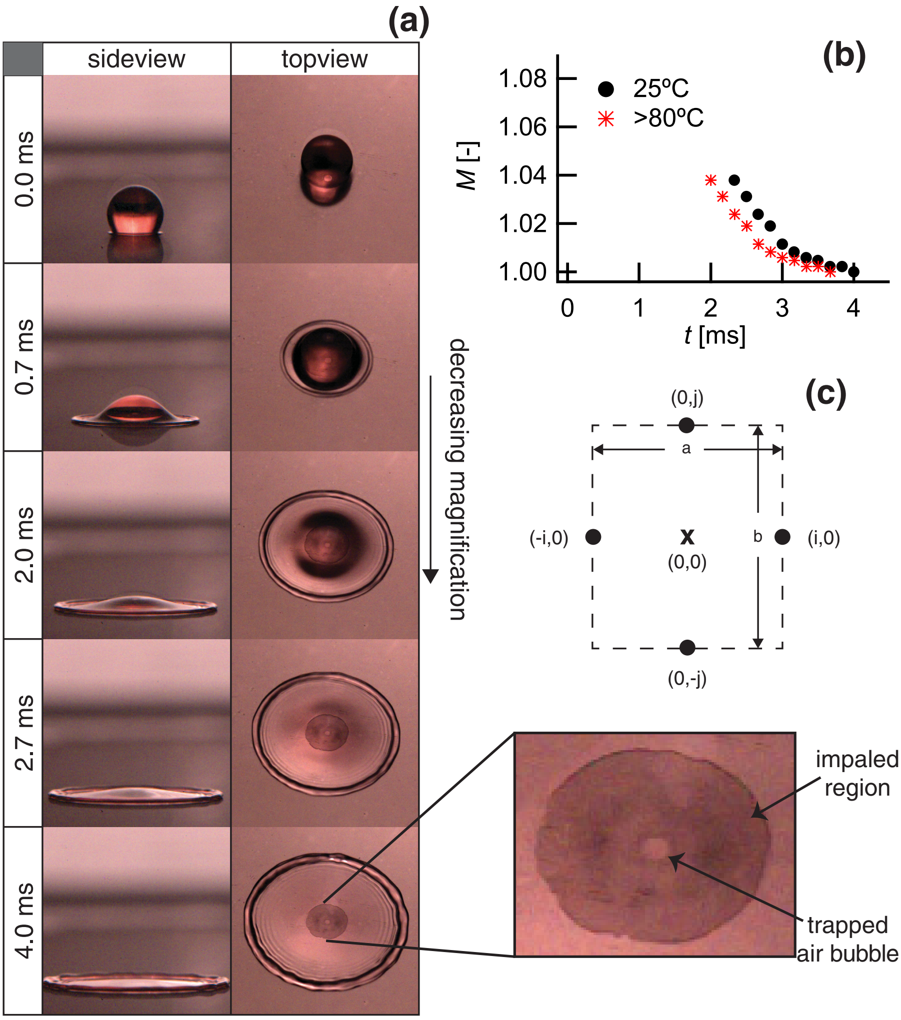

FIG. 3. (a) Droplet spreading following impingement at We ∼ 190 and ambient temperature ($T_s \sim 25\,^\circ$C). (b) Temporal magnification of impaled area due to droplet curvature at room temperature (•) and on a heated substrate $T > 80\,^\circ$C ($*$). (c) Schematic of stencil used to map the extent of magnification during initial droplet impingement.

temperature, a silicon wafer was coated with a thin film of known emissivity (0.96) and placed on top of the aluminum block. Its temperature, as measured with a thermal camera, was nominally 4 °C lower than the thermocouples in the range $80 < T_s < 100\,^\circ$C, where T_s will denote the substrate temperature prior to droplet contact from now on.

To capture dewetting events, a second high speed camera was positioned at an inclination of 70 ° above the horizontal, as to not interfere with the falling droplet. Figure 3(a) shows a representative impingement event on the 16p18h substrate at room temperature from both camera views. A dark region in the center of the droplet can be observed in the later panels of the top view sequence, which has already been established as impaled liquid on SH substrates of similar scale [35,48]. The impaled region is not visible in the first two frames because the drop obscures the view during the initial moments of impingement. Thus, data reported in this work entail dynamics for $t > 2.5$ ms (at room temperature) and $t > 2$ ms (for $T_s > 80\,^\circ$C), due to a decrease of viscosity of the droplet

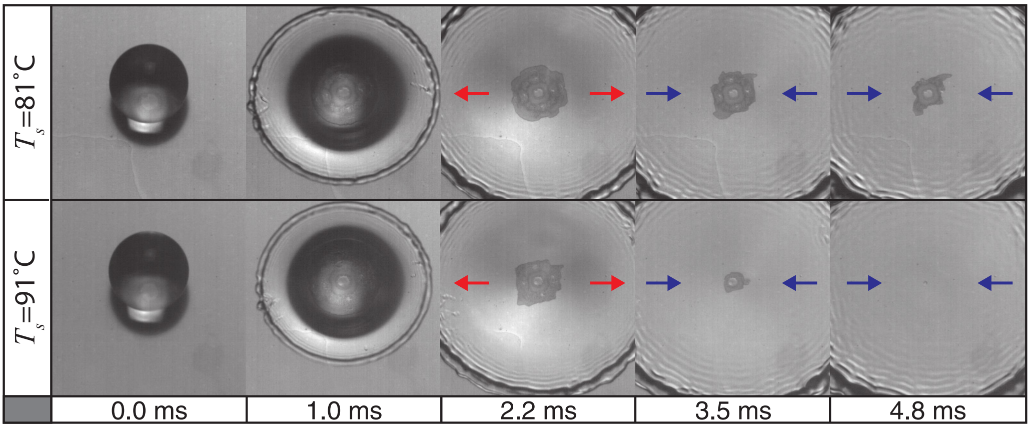

FIG. 4. Dewetting process during impingement on a 16p18h substrate with $T_s = 81$ and 91 °C. In both cases, the impaled region gets smaller with time, but dewetting occurs at a faster rate for $T_s = 91$ °C such that a complete transition from the Wenzel to the Cassie state has occurred by 4.8 ms. Arrows indicate whether the lamellar ring is moving away or towards the center.

and hence slightly faster spreading at higher T_s. After this point and up to ∼3.5 ms, the lingering curvature of the droplet optically magnifies the area of impalement. This effect endures until the droplet becomes flat in the thin film and is quantified below. An edge-finding algorithm based on pixel-value gradient detection was used to measure the impaled area, A, as a function of time [note A is constant in Fig. 3(a)] not including the air bubble at the center, which forms due to air entrapment. The volume of the impaled liquid, Ω, was obtained by $\Omega = A(1 - \phi_s)h$. Generally, 10 trials were conducted for each scenario (a given surface at a given temperature). Overall uncertainty, including randomized uncertainty due to scatter, of penetrated volume at any time was obtained based on a 95% confidence level and resulted between 2.7% and 4.3% across all cases.

During the initial stages of impingement, the top of the droplet forms a concave interface (see the first four images of the sequence shown in Fig. 3), with a radius of curvature, $\mathcal{R}(t)$. Given the difference in index of refraction between water ($n_w = 1.33$) and air ($n_a = 1.00$), the concavity acts like a magnifying lens such that the high speed camera detects a larger impaled region than actually exists. Magnification endures until the interface becomes flat (i.e., $\mathcal{R} \to \infty$). To obtain the temporal magnification, $M(t)$, four small dots (∼0.1 mm) were marked on a superhydrophobic substrate creating a square similar in size to the impaled area at $(-i,0)$, $(i,0)$, $(0,j)$, and $(0,-j)$ around the center of the impingement as shown in Fig. 3(c). Each of the four points were then tracked with the top camera during impingement and the temporal evolution of the area, $A_s = a \times b$, was divided by the unmagnified area to obtain M at each time step. Results are shown in Fig. 3(b), where $t = 0$ corresponds to the time when the droplet first contacts the substrate. The symbols represent an average of five tests. Results show that magnification is modest (<5%) throughout the spreading event and under 1% after 3.5 ms from impingement.

III. EXPERIMENTAL RESULTS

Here, we quantify the effects that superhydrophobic architecture and substrate temperature have on the Wenzel to Cassie transition (dewetting) during droplet impingement. Dewetting rates are considered up to the point when the retracting droplet obscures the impaled region prior to rebound (typically ∼8 ms). Two representative image sequences of dewetting events on the 16p18h substrate at 81 and 91 °C are shown in Fig. 4. The data for the 81 °C case shows that the impaled region, which can be clearly seen by the third panel ($t = 2.2$ ms), is shrinking with time, indicating that dewetting is occurring. However, some liquid remains trapped in the pillars at the end of the event. For the

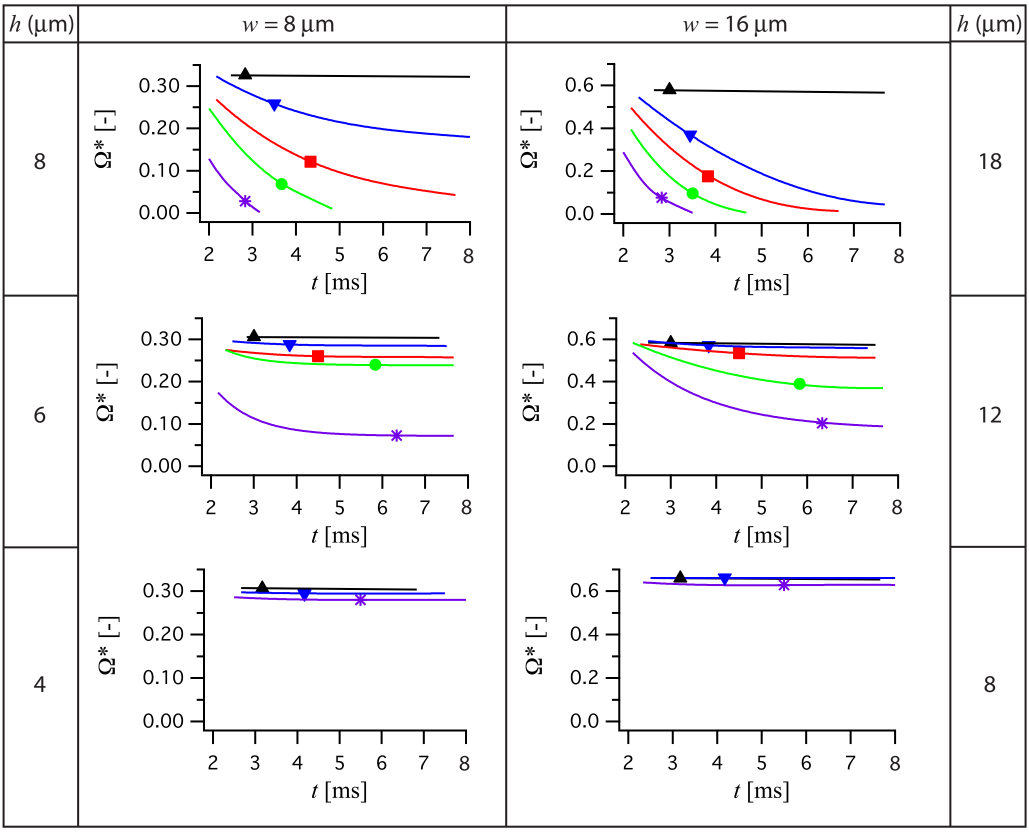

FIG. 5. Temporal evolution of Ω^* for the 8 μm (left) and 16 μm pitch (right) substrates. On the left, pillar height is 4 μm ($r = 1.59$), 6 μm ($r = 1.88$), and 8 μm ($r = 2.18$) from bottom to top, while on the right, pillar height is 8 μm ($r = 1.59$), 12 μm ($r = 1.88$), and 18 μm ($r = 2.33$) from bottom to top, respectively. ▲, ▼, ■, ● and ✳ represent $T_s = 25, 81, 86, 91$, and 96 °C.

91 °C case, the rate of dewetting is faster and the impaled liquid completely vanishes at $t = 4.8$ ms. We note that dewetting is not necessarily achieved on all substrates or at all temperatures, as will be shown later. The arrows in the last three panels of the top sequence indicate whether the droplet is spreading (arrows point outwards) or retracting (arrow point inwards), thus illustrating that dewetting is not influenced by whether the droplet is spreading or retracting. Finally, the images reveal that although impingement is axisymmetric, the square lattice arrangement of the micropillars causes the impaled region to deviate from a circular shape and exhibit sharp corners, in accordance with the work of Reysatt *et al.* [35].

Results that are shown in Fig. 5 characterize the temporal dewetting dynamics for substrate temperatures of $25 < T_s < 96\,^\circ$C. The temporally varying volume of penetrated or impaled liquid is normalized by a characteristic volume based on the projected area of the droplet and the height of the pillar array for the given substrate, which yields the normalized volume, $\Omega^* = 4\Omega/(\pi D_o^2 h)$. The three panels on the left present data for the 8 μm pitch substrates with pillar heights of 8 μm (top), 6 μm (middle) and 4 μm (bottom), while the three panels on the right represent the 16 μm pitch substrates with pillar heights of 18 μm (top), 12 μm (middle) and 8 μm (bottom). Each curve is the average of ten trials at the same conditions, as explained in Sec. II.

First, dewetting behavior for the 8 μm pitch substrates is discussed. The data of the top left panel (8p8h substrate) show that at a substrate temperature of 25 °C (room temperature) dewetting does not occur (normalized impaled volume is invariant with time). At $T_s = 81\,^{\circ}\mathrm{C}$, dewetting occurs with Ω^* decreasing with time and the rate of dewetting increasing with increasing T_s. At $T_s = 91$ and $96\,^{\circ}\mathrm{C}$, the impaled volume transitions completely from the Wenzel to the Cassie state by approximately 5 and 3 ms, respectively. It is also noted that the initial normalized dewetting rate, $d\Omega^*/dt$ (at $t \sim 2$ ms), increases with increasing substrate temperature, and this behavior is consistent with all substrates considered.

As pillar height decreases at constant pitch, dewetting becomes less sensitive to temperature. For the 8p6h substrate, dewetting does not occur for any temperatures explored up to $T_s = 81\,^{\circ}\mathrm{C}$, and only modest dewetting is evident for the $T_s = 86$ and $91\,^{\circ}\mathrm{C}$ cases. At $T_s = 96\,^{\circ}\mathrm{C}$, dewetting is pronounced, with only 29% of the initial impaled volume remaining in the impaled state after 8 ms. The nature of the decrease in Ω^* with time is different for this scenario than for the 8p8h substrate. For $T_s \geqslant 86\,^{\circ}\mathrm{C}$, the impaled volume decreases but then levels off and ceases to change (dewetting stops) with time at $t \sim 4$ ms, and this behavior is more evident as T_s increases further. The data in the bottom left panel show that the impaled volume is unchanging with time (no dewetting occurs) for all temperatures explored for the 8p4h substrate, further demonstrating the observation that dewetting rates decrease with decreasing pillar height.

Similar dewetting trends are observed on the 16 μm pitch substrates (right panels of Fig. 5). For the 16p18h case, no dewetting occurs at room temperature, but dewetting rates increase significantly for elevated substrate temperatures. Complete dewetting is observed for substrate temperatures of 86, 91, and $96\,^{\circ}\mathrm{C}$ at 6.7, 4.8, and 3.7 ms, respectively. Similar to the 8p8h surface, $d\Omega^*/dt$ (at $t \sim 2$ ms) increases with increasing temperature. On the 16p12h substrate, the rate of dewetting is not as great as on the 16p18h substrate and only becomes apparent at $T_s = 86\,^{\circ}\mathrm{C}$, with the dewetting rate increasing for $T_s = 91$ and $96\,^{\circ}\mathrm{C}$. For these two temperatures, the final impaled volumes are 69% and 36% of the initial impaled value for the room temperature scenario. When dewetting occurred for the 16 μm pitch substrates, the impaled volume always decreased with time and no plateauing trends were observed, in contrast to the 8p6h substrate. Finally, dewetting did not occur for the 16p8h substrate at any temperature. Data for the 16p16h substrate are not shown in Fig. 5 for clarity, but lie between the data for the $h = 12$ and 18 μm cases.

In summary, dewetting rates increase with increasing h and T_s, although no dewetting occurs for the shortest pillar height (for either pitch) at any T_s, or for the lowest substrate temperature (ambient) at any h. Both the 8 and 16 μm pitch substrates yielded similar behavior at corresponding r values (i.e., 8p4h and 16p8h, 8p6h and 16p12h, etc; see Table I). Because dewetting dynamics were captured during droplet spreading and retracting (i.e., prior to droplet rebound), the droplet can be expected to rebound without pinning due to impalement for complete dewetting cases.

In the next section, a thorough analysis of the observed behavior is provided. We first conclude this section by introducing the idea of a wetted disk of effective radius R_ϵ, which will be necessary in the analysis. Photographs shown earlier depicted the impalement region to be initially nearly axisymmetric, but that the symmetry evolved during dewetting into a more “square” shape due to the square lattice arrangement of the micro-pillars. Shown in Fig. 6(a) are images of the dewetting event for the 8p8h substrate at a surface temperature of $91\,^{\circ}\mathrm{C}$ (top sequence) and a corresponding representative axisymmetric shape (bottom sequence) for the upcoming analysis. Due to the entrapped air bubble described previously, there was no impalement in the center of the impaled region (as shown in the images), with the radius of this region denoted as R_b. The total impaled volume was obtained by integrating over the dark region to determine the total impaled area, which is then multiplied by the pillar height. An effective radius of the impaled region can thus be computed as $R_\epsilon = \sqrt{\Omega/[\pi(1-\phi_s)h]}$, and this will be important for the analysis that is conducted in the following section. A normalized effective radius $[R_\epsilon^* = R_\epsilon/(D_o/2)]$ was computed as a function of time for all cases considered.

Shown in Fig. 6(b) is R_ϵ^* as a function of time for the 16p18h substrate at $T_s = 86\,^{\circ}\mathrm{C}$, with ten individual trials included. The data reveal excellent repeatability for all trials and shows a linearly decreasing effective radius with increasing time over the majority of the dewetting event. Deviation from linearity occurs only as R_ϵ approaches the radius of the air bubble trapped in the center, where

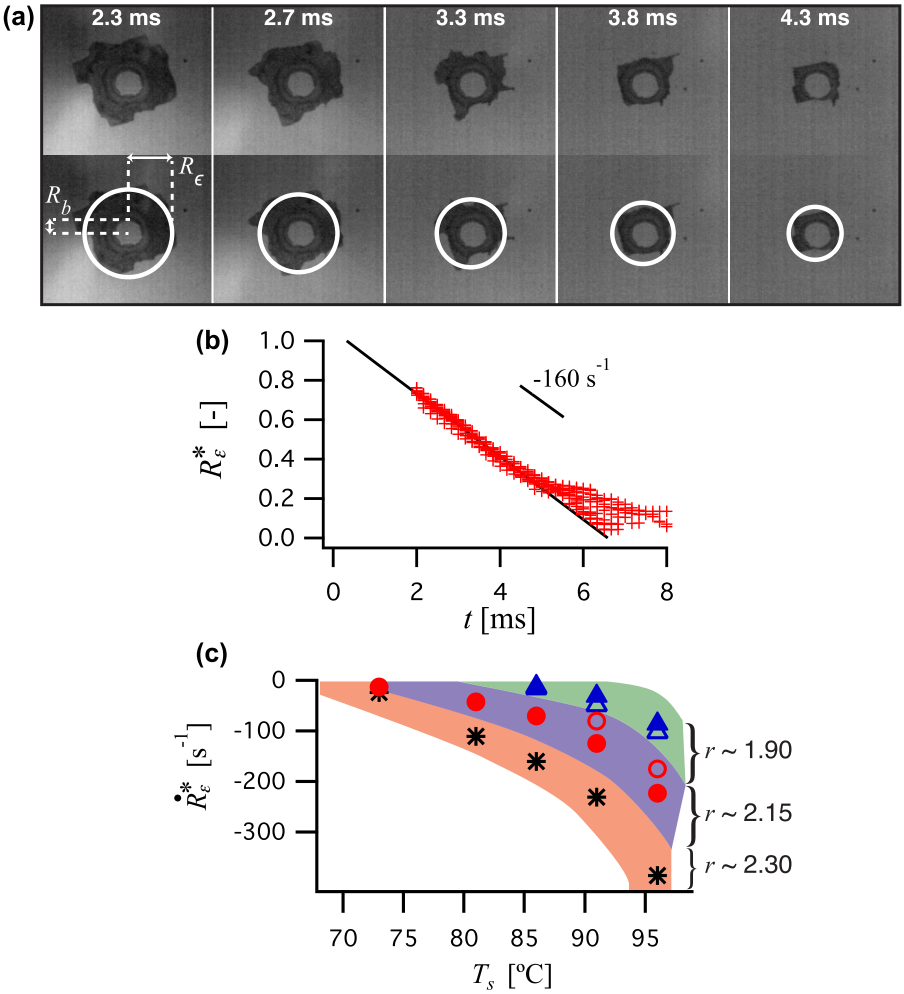

FIG. 6. (a) Image sequence of dewetting event for the 8p8h substrate at 91 °C. Overlaid circle of effective radius R_ϵ used in evaporation and force balance models (bottom sequence). (b) Temporal decay of R^*_ϵ for ten data sets on the 16p18h substrate at $T_s = 86\,^\circ\mathrm{C}$. (c) $\dot{R}^*_\epsilon$ as a function of T_s for the 8p6h (▲), 16p12h (△), 8p8h (●), 16p16h (○), and 16p18h (✳) substrates (background color added to emphasize separation due to increasing r values).

interaction of this bubble and the effect of individual pillars becomes important. Also shown in the figure is a linear fit to the data from ∼2 to ∼5 ms. The implication of this is that the dewetting rate $dR^*_\epsilon/dt \equiv \dot{R}^*_\epsilon$ is constant over most of the dewetting process. The data for all scenarios exhibited a similar linear relationship, although with a different slope. The behavior of $\dot{R}^*_\epsilon$ is shown in Fig. 6(c) as a function of substrate temperature for all substrates where dewetting occurred. The figure shows that, for a given T_s, dewetting rates increase for increasing r values, as expected.

IV. ANALYSIS

Three independent mechanisms exist that may cause dewetting to occur: buoyancy-driven convection, evaporation, and a force resulting from a surface energy gradient between the Wenzel and Cassie states. First, a temperature gradient (decreasing in the vertical direction away from the wall) exists within the impaled liquid and could yield bulk movement of the liquid due to varying

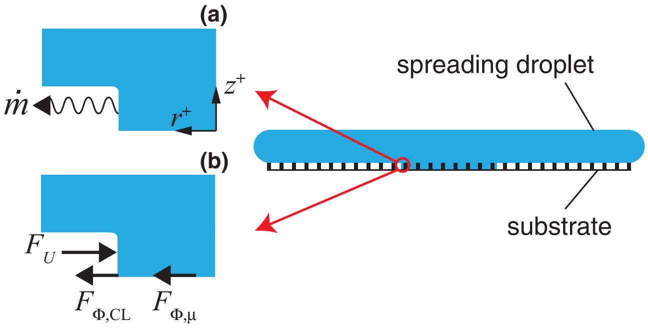

FIG. 7. Schematic representation of dewetting models for evaporation (a) and a force balance (b). Pillars are not shown on schematics on the left for clarity.

density. A buoyancy-induced force would scale as $\rho\beta\Delta T g\Omega$ with ρ, β, ΔT, and g representing liquid density, the volumetric thermal expansion coefficient, temperature differential, and acceleration due to gravity. However, dewetting due to buoyancy effects is unlikely because of the thinness of the impaled liquid film, h, embedded in the pillar array. Further, although a temperature gradient may induce warmer liquid at the bottom to flow in the direction of decreasing temperature, the rising liquid would be instantaneously replaced by descending colder liquid. Thus, buoyancy will not be considered here. Secondly, evaporation of the impaled liquid through the peripheral liquid-air interface is expected to increase with increasing temperature and increasing liquid-gas interfacial area ($\propto h$), both of which agree with trends exhibited by the data. The last mechanism exists because of a surface energy gradient between the Wenzel and Cassie states, which induces an inward pull (in the negative radial direction) on the impaled liquid. Figure 7 shows schematic illustrations of evaporation and a balance of surface energy and dissipative forces acting on the impaled thin film of liquid. To quantify the extent to which these mechanisms influence dewetting, scaling arguments are considered further below.

A. Evaporation

Evaporation around the periphery of the impaled liquid at the liquid-gas interface is considered by assuming the impaled volume of liquid is axisymmetric with effective radius R_ϵ and liquid-gas interfacial area $A_p = 2\pi R_\epsilon h(1-\phi_p)$, where $\phi_p = d/w$ is the solid fraction around the periphery of the effective impaled disk. The rate of evaporation, $\dot{m}$, in this scenario is governed by

$$\dot{m} = \bar{h} A_p(\rho_{s@T_s} - \rho_{s@T_o}), \tag{1}$$

where $\bar{h}$ is an average mass transfer coefficient and the term in parentheses represents the difference in density of the saturated vapor at the substrate temperature, T_s, and ambient temperature, T_o, and is the driving potential. To obtain an estimate of the highest evaporation rates possible, forced convection was assumed. Thus, an average mass transfer coefficient, $\bar{h}$, can be estimated via the following empirical relation for forced convection over a flat interface [49]

$$\frac{\bar{h}L}{D_{AB}} = 0.664\,\mathrm{Re}_e^{1/2}\,\mathrm{Sc}^{1/3}. \tag{2}$$

Here, L represents the streamwise length of the flow at the liquid-air interface, D_{AB} is the binary diffusion coefficient of water vapor in air (adjusted for local pressure, $D_{AB} = 4.2 \times 10^{-5}$ m^2/s), $\mathrm{Re}_e = \bar{V}L/\nu$ is the Reynolds number, and $\mathrm{Sc} = \nu/D_{AB}$ is the Schmidt number (ν_{air} is the kinematic viscosity of air and $\bar{V}$ is the velocity of the flow).

Air under the droplet is driven by the spreading motion of the droplet. Because the droplet impacts the substrate with velocity V_o, we assume $\bar{V} \sim V_o \sim 2$ m/s. The characteristic length in the direction of the air flow, L, is the height of the interfacial area through which evaporation occurs, $L \sim h$. The tallest pillars tested in this work were 18 μm, which yields $\mathrm{Re}_e \sim \mathrm{Sc} \sim 1$. Finally, a representative R value from experimental observations is 10^{-3} m. Use of these values and Eqs. (1) and (2) yields an upper bound for the evaporation rate of $\sim 10^{-8}$ kg/s. This value is at least two orders of magnitude smaller than typical measured dewetting rates and as a result we conclude that evaporation is not the dominant mechanism. However, it is possible that evaporation around the periphery may initially trigger dewetting by releasing the impaled liquid from a "pinned" state. Next, we consider the forces at play during the dewetting event.

B. Surface-tension/dissipation-force balance

A force balance in the radial direction (see Fig. 7 for the coordinate system) on a disk of effective radius R_ϵ can be expressed as $F_U = \Sigma F_{\Phi,i}$, where F_U represents the force due to a surface energy gradient between the Wenzel and Cassie state and $\Sigma F_{\Phi,i}$ includes all dissipative forces. Inertia is neglected because the "system" consists of only the thin disk of impaled liquid and not the entire droplet.

The total surface energy includes interactions between all immiscible interfaces (solid-gas, solid-liquid, and liquid-gas) and is obtained by multiplying interfacial areas by their respective surface tensions [23,32,33,50]. When liquid dwells in the Wenzel state, its total surface energy can be expressed as [32,33]

$$U_w = \gamma_L \pi R_\epsilon^2 r + \sigma 2\pi R h \phi_p, \tag{3}$$

where γ_L and σ are liquid-solid and liquid-gas surface tension values. The second term on the right-hand side of (3) is very small compared to the first term for the current situation where $h \ll R_\epsilon$ and is neglected. Energy in the Cassie state can also be easily defined and simplified via Young's relation, $\cos\theta_e = (\gamma_G - \gamma_L)/\sigma$, as [32,33]

$$U_c = \pi R_\epsilon^2 [\sigma(1-\phi_s) - \sigma\phi_s \cos\theta_e + \gamma_G r], \tag{4}$$

where γ_G is solid-air surface tension.

It is the difference of the foregoing energy states that either promotes or resists dewetting (the system will tend towards the lower energetic state). Thus, it is useful to define an effective surface energy state, U_{eff}, as the difference between the two [32,51],

$$U_{\mathrm{eff}} \equiv U_w - U_c = -\pi R_\epsilon^2 \sigma [\cos\theta_e (r - \phi_s) + 1 - \phi_s], \tag{5}$$

where we expect dewetting to occur for $U_{\mathrm{eff}} > 0$ and the rate of dewetting to increase with increasing U_{eff}. The presence of the air bubble in the center of the impaled region is easily taken into account by redefining U_{eff} as

$$U_{\mathrm{eff}} = -\pi \left(R_\epsilon^2 - R_b^2\right) \sigma [\cos\theta_e (r - \phi_s) + 1 - \phi_s], \tag{6}$$

where R_b is the radius of the bubble and observations reveal it to be essentially constant. A force stemming from U_{eff} can be obtained by $F_U = -\nabla U_{\mathrm{eff}}$ [51,52] to yield,

$$F_U = 2 R_\epsilon \pi \sigma \xi. \tag{7}$$

In the above expression, $\xi = [\cos\theta_e (r - \phi_s) + 1 - \phi_s]$. F_U acts in the negative radial direction—thus facilitating dewetting—when $\xi < 0$. Pillar height, h, comes into play in Eq. (7) through the roughness factor ($r = 1 + \pi d h / w^2$). Increasing h effectively increases the magnitude of F_U (since $\theta_e > \pi/2$), and thus provides an explanation for the experimental observations that dewetting rates increase with pillar height due to an increasing driving force. Equation (7) further reveals that the dewetting rates observed from the experiments does not depend on pillar height exclusively, but rather on the roughness factor, which explains why substrates with similar r values exhibited similar behavior.

The Young contact angle, θ_e, can have an instantaneous value within the hysteresis range for a given liquid-solid interface. For the present surfaces, the interface is water-Teflon and the measured

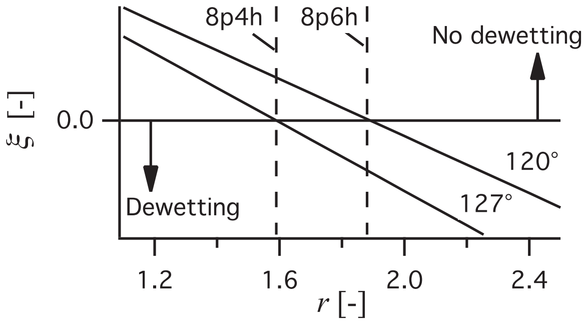

FIG. 8. Experiments revealed that dewetting ($\xi < 0$) begins somewhere between $1.59 < r < 1.88$ (vertical dashed lines) indicating that the contact angle adopted at the periphery of impalement lies between 120° and 127° (solid lines).

advancing and receding values show that $113^\circ < \theta_e < 128^\circ$. Given the nature of the experiments it is impossible to know the instantaneous value of θ_e as the impaled liquid retreats through the pillar forest. To demonstrate the sensitivity of θ_e on the driving force, ξ is shown as a function of r in Fig. 8 for $\theta_e = 120^\circ$ and 127°. If ξ is positive, the driving force from Eq. (7) is positive and dewetting is not expected to occur, while the converse is true for negative values of ξ. For a given value of θ_e, ξ will be positive at small roughness values (no dewetting) and becomes negative as the roughness increases. Since roughness increases with pillar height, Cassie state favorability and hence dewetting is promoted with increasing pillar height for any pitch as was observed experimentally. Furthermore, at roughness values in the range 1.6–1.9, small changes in the instantaneous value of θ_e can lead to the value of ξ changing from a positive to a negative, or vice-versa. An implication of this is that the dewetting rate for a particular substrate can change with time, and that small changes in θ_e can result in dewetting stopping. We hypothesize that this is the dynamic at play for the substrates where dewetting was observed initially, followed by a dewetting rate that vanished.

Recall from the data of Fig. 5 that dewetting first began at roughness values between $r = 1.59$ (the 8p4h or 16p8h substrate, neither of which ever dewet) and 1.88 (the 8p6h substrate). Dashed vertical lines are depicted in Fig. 8 corresponding to these roughness values. For roughness values greater than $r = 1.88$, dewetting always occurred (with the rate dependent on temperature) and for roughness values less than $r = 1.59$, dewetting was never observed. The magnitude of ξ at $\theta_e = 127^\circ$ changes sign at $r = 1.59$ and at $\theta_e = 120^\circ$ the change in sign occurs at 1.88. These values of θ_e lie within the measured hysteresis range and we safely conclude that the instantaneous value of θ_e during the dewetting process is between 120° and 127°.

The receding impaled liquid results in a moving three-phase (solid-liquid-gas) contact line, hereafter simply referred to as “contact line”, that extends around the periphery of the impaled region. The motion of moving contact lines result in large dissipation rates due to velocity gradients within the liquid domain (hydrodynamical dissipation), friction due to molecular hopping at the contact line (generally referred to as nonhydrodynamical dissipation having been derived from Molecular Kinetic Theory, MKT) and a precursor film. Precursor film dissipation has only been deemed important at moving contact lines of completely wetting liquids [53] and is thus neglected here.

A hydrodynamic dissipation force due to velocity gradients at the bottom surface and adjacent to the vertical pillars scales as $\mu \dot{R}_\epsilon R_\epsilon$, where μ is the viscosity of the impaled liquid, R_ϵ is the effective radius of the impaled (wet) region, and $\dot{R}_\epsilon$ is the dewetting rate. Equating this dissipation scaling with the driving force due to surface tension gradients given in Eq. (7) yields the following scaling

$$\mu \dot{R}_\epsilon \sim \sigma \xi \tag{8}$$

Because the driving and dissipative forces are linearly dependent on R_ϵ, the scaling suggests $\dot{R}_\epsilon$ is constant for a given scenario. Common models for liquid viscosity are of the form $\mu \sim 10^{B/(T-C)}$ where T is the absolute temperature of the impaled liquid and B and C are empirically-derived constants of best fit for the distribution of dynamic viscosity with temperature [54]. Substituting this temperature dependency for viscosity into (8) and rearranging suggests that all data should collapse in the following manner

$$\frac{\dot{R}_\epsilon}{\xi} \sim 10^{-B/(T-C)} \tag{9}$$

where σ has been assumed to be constant and is dropped from the scaling. Shown in the top panel of Fig. 9 is a comparison of the scaling of Eq. (9) with the experimental data, where $\dot{R}_\epsilon/\xi$ is plotted as a function of the surface temperature, where ξ was determined at a constant value of $\theta_e = 123.5^\circ$. For the scaling, coefficients for the viscosity of water obtained from literature are utilized, with $B = 247.8$ K and $C = 140$ K [54] and T being set to the measured substrate temperature for each scenario. The experimental data for all scenarios considered (shown in symbols) collapse to a similar power-law curve. The scaling of Eq. (9) is also shown in the figure and although the model also suggests a power relationship (governed by the dependence of viscosity in temperature), it does not capture the trend followed by the experimental data, which exhibits a much stronger dependence on temperature. This mismatch between the scaling and the data indicates that hydrodynamic dissipation is not the dominant mode of dissipation during dewetting.

We now consider dissipation caused by the moving contact line. Derivation of dissipation at the contact line due to molecular hopping is extensive and stems from Eyring's molecular-kinetic theory (MKT) model [55]. Blake *et al.* adapted this MKT model and developed an expression for a moving contact line dissipative force [56], which is used here. When the contact angle at the moving contact line is similar to the static contact angle, which is the case here, the dissipative force can be expressed as [57–59]

$$F_{\Phi,\mathrm{CL}} = 2\pi R_\epsilon \dot{R}_\epsilon \frac{\hbar}{\lambda^3} e^{\Delta G_w/Nk_BT}, \tag{10}$$

where λ is the individual molecular displacement, k_B is the Boltzmann constant, ΔG_w is the activation free energy of wetting, N is Avogadro's number, and $\hbar$ is Planck's constant. The downside of this theoretical manifestation is the difficulty of comparing it with experiments. Because λ and ΔG_w are usually not known *a priori*, they are obtained by curve fitting empirical data of a specific liquid-solid-gas interaction. Tabulated values vary widely and available data only exists for very specific scenarios at specific temperatures (normally room temperature) [56–60]. Furthermore, care must be taken when interpreting and utilizing such empirical results due to the sensitivity of these constants: λ is raised to the third power and ΔG_w dwells inside an exponential. For simplicity and to form a scaling argument, λ is discarded from Eq. (10), thus giving the following scaling:

$$F_{\Phi,\mathrm{CL}} \sim R_\epsilon \dot{R}_\epsilon e^{\Delta G_w/Nk_BT} \tag{11}$$

The driving force, F_U, is now balanced with the triple line dissipative force to yield

$$\dot{R}_\epsilon \sim \xi\Phi \tag{12}$$

with $\Phi = e^{-\Delta G_w/Nk_BT}$. This relation also indicates that dewetting speed is constant for a given scenario (i.e., no dependance on R_ϵ), which agrees with the experimental behavior already discussed [Fig. 6(b)]. Furthermore, the scaling of Eq. (12) also suggests that the experimental data should collapse as a function of temperature with $\dot{R}_\epsilon/\xi$.

The middle panel of Fig. 9 again shows the experimental results for $\dot{R}_\epsilon^*/\xi$ as a function of T_s. The experimental data collapses and agrees with the scaling argument in Eq. (12) with $\Delta G_w = 131 \times 10^3$ J mol^{-1}. This value of ΔG_w was obtained by performing a least squares fit to the experimental data. A value for ΔG_w is not available from the literature for a water-Teflon-air interface at the specific temperatures explored, however, the value obtained here is within a factor of three to

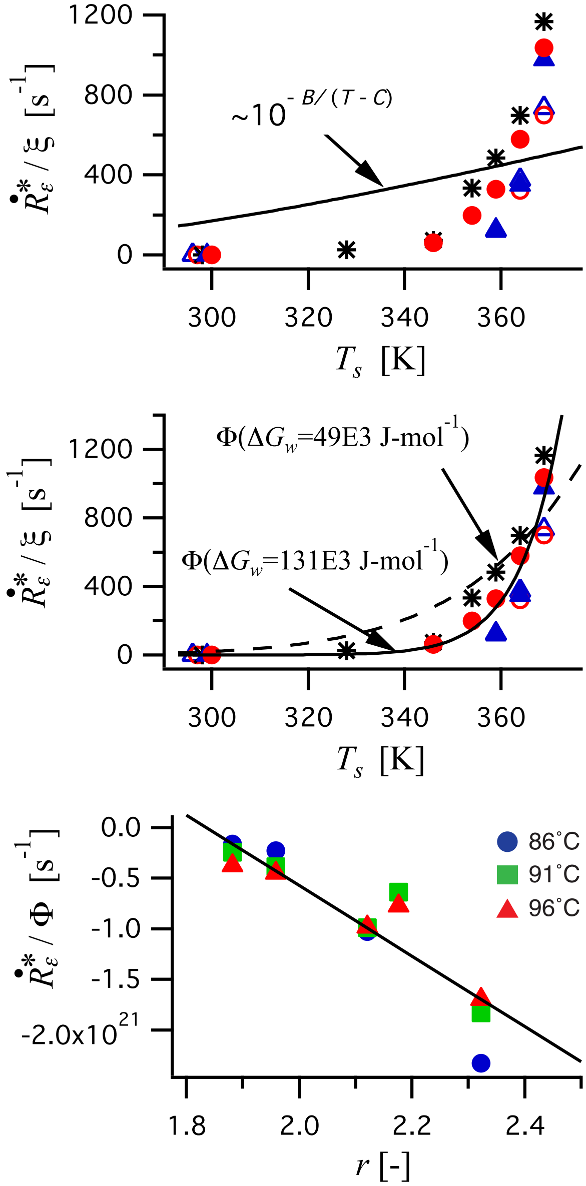

FIG. 9. Top and middle panels: $\dot{R}^*_\epsilon/\xi$ as a function of T_s for all scenarios considered where dewetting occurred with $\xi(\theta_e = 123.5^\circ)$. Symbols represent the experimental data and follow the same convention used in Fig. 6(c). In the top panel, the solid curve represents the scaling of Eq. (9), while in the middle panel the solid and dashed curves represent the scaling of Eq. (12) for two different ΔG_w values as depicted. Bottom panel: $\dot{R}^*_\epsilon/\Phi$ with $\Delta G_w = 131 \times 10^3$ J mol^{-1} as a function of r.

a published value for a glycerol/water mixture (70% aqueous) on Mylar polyester tape (also a hydrophobic interaction), where $\Delta G_w = 49 \times 10^3$ J mol^{-1} [56]. The scaling of Eq. (12) with this value of ΔG_w is also shown in the middle panel of Fig. 9 for comparative purposes, where the dependence on temperature is not as great as demonstrated by the experimental data. Finally, $\dot{R}^*_\epsilon$ normalized by the exponential of Eq. (12) is shown as a function of r in the bottom panel of Fig. 9.

The experimental data collapses into an approximately linear decay as a function of r, as suggested by Eq. (12), where $\xi \propto r$.

The models developed in this section arise from a force balance between the driving force generated by the surface tension gradient that exists between the Wenzel and Cassie state and a dissipation force. The results suggest that hydrodynamic dissipation exerts only a small influence, while the contact line dissipation plays the predominant role in the dissipation and resistance to dewetting. The scale analysis (contact line dissipation) agrees very well with the experimental observations that increasing pillar height and increasing substrate temperature increase dewetting rates. These two occur for different reasons, the former because of an increase in the driving force, while the latter because of a decrease in dissipation.

V. CONCLUSION

In this paper the transient process where a localized Wenzel state incurred during droplet impingement recedes or "dewets" back to the Cassie state has been explored. Unlike other mechanisms previously considered for transition from the Wenzel to Cassie state, which aggressively affect the flow, such as boiling or vibrations, the one discussed here achieves dewetting passively. Experiments reveal that dewetting rates are strongly dependent on the substrate temperature and micro-pillar height. The influence that both of these parameters exert on the process were quantified over a temperature range of 25 to 96 °C, pillar height range from 4 to 18 μm, and for two pitch values, 8 and 16 μm. Two dewetting mechanisms were considered to explain the dewetting behavior, with one based on evaporation and the other based on a force balance. Evaporation was found to exert negligible influence. The force balance equated the driving force, based on a gradient between the Wenzel and Cassie energy states with dissipation. Hydrodynamic and nonhydrodynamic (based on molecular hopping at the triple contact line) dissipations were considered (with forces that act in opposition to the dewetting motion). A scaling argument revealed that hydrodynamic dissipation plays a minor role and that nonhydrodynamic dissipation exerts dominant influence. The overall results can be summarized as follows:

(1) The rate at which dewetting occurs increases with increasing substrate temperature and pillar height.

(2) Both the experiments and scaling suggest that geometrical parameters (such as pillar height or pitch) are not individually important, but a combination in the form of the roughness factor governs the dynamics.

(3) A force resulting from an energy gradient between the Wenzel and Cassie states drives dewetting, while contact line resistance inhibits the flow.

(4) The scaling provides a physical explanation for the experimental observations: Increasing h induces dewetting due to an increased driving force, while increasing T_s also induces dewetting but due to decreased dissipation.

These findings have broader implications in the design and commercialization of superhydrophobic surfaces for varying applications, especially those focused on single droplet or multidroplet mobility. Further research should include microfeatures of differing geometry (square posts, ribs, etc.) and different liquid-solid hydrophobic interactions.

ACKNOWLEDGMENT

The authors gratefully acknowledge support by the National Science Foundation under Grant No. (CBET-1235881).

---

[1] R. N. Wenzel, Resistance of solid surfaces to wetting by water, Ind. Eng. Chem. **28**, 988 (1936).
[2] A. Cassie and S. Baxter, Wettability of porous surfaces, Trans. Faraday Soc. **40**, 546 (1944).

[3] S. Arya, S. Khan, A. Vaid, H. Kour, and P. Lehana, Microfluidic mechanics and applications: A review, J. Nano Electron. Phys. **5**(4), 04047 (2013).

[4] D. Quéré, Wetting and roughness, Annu. Rev. Mater. Res. **38**, 71 (2008).

[5] S. Herminghaus, Roughness-induced non-wetting, Europhys. Lett. **52**, 165 (2000).

[6] J. T. Pearson, D. Maynes, and B. W. Webb, Droplet impact dynamics for two liquids impinging on anisotropic superhydrophobic surfaces, Exp. Fluids **53**, 603 (2012).

[7] Z. Guo and W. Liu, Biomimic from the superhydrophobic plant leaves in nature: Binary structure and unitary structure, Plant Sci. **172**, 1103 (2007).

[8] J. C. Bird, R. Dhiman, H. Kwon, and K. K. Varanasi, Reducing the contact time of a bouncing drop, Nature (London) **503**, 385 (2013).

[9] M. K. Tiwari, I. S. Bayer, G. M. Jursich, T. M. Schutzius, and C. M. Megaridis, Highly liquid-repellent, large-area, nanostructured poly(vinylidene fluoride)/poly(ethyl 2-cyanoacrylate) composite coatings: Particle filler effects, ACS Appl. Mater. Interfaces **2**, 1114 (2010).

[10] L. Feng, S. Li, Y. Li, H. Li, L. Zhang, J. Zhai, Y. Song, B. Liu, L. Jiang, and D. Zhu, Super-hydrophobic surfaces: From natural to artificial, Adv. Mater. **14**, 1857 (2002).

[11] D. Maynes, K. Jeffs, B. Woolford, and B. W. Webb, Laminar flow in a microchannel with hydrophobic surface patterned microribs oriented parallel to the flow direction, Phys. Fluids **19**, 093603 (2007).

[12] B. Woolford, D. Maynes, and B. W. Webb, Liquid flow through microchannels with grooved walls under wetting and superhydrophobic conditions, Microfluid. Nanofluid. **7**, 121 (2009).

[13] B. Woolford, J. Prince, D. Maynes, and B. W. Webb, Particle image velocimetry characterization of turbulent channel flow with rib patterned superhydrophobic walls, Phys. Fluids **21**, 085106 (2009).

[14] J. Davies, D. Maynes, B. W. Webb, and B. Woolford, Laminar flow in a microchannel with superhydrophobic walls exhibiting transverse ribs, Phys. Fluids **18**, 087110 (2006).

[15] R. Blossey, Self-cleaning surfaces - virtual realities, Nat. Mater. **2**, 301 (2003).

[16] J. B. Boreyko and C.-H. Chen, Restoring Superhydrophobicity of Lotus Leaves with Vibration-Induced Dewetting, Phys. Rev. Lett. **103**, 174502 (2009).

[17] J. Prince, J. Crockett, and D. Maynes, Jet impingement and the hydraulic jump on horizontal surfaces with anisotropic slip, Phys. Fluids **26**, 042104 (2014).

[18] D. Maynes, B. W. Webb, J. Crockett, and V. Solovjov, Analysis of laminar slip-flow thermal transport in microchannels with transverse rib and cavity structured superhydrophobic walls, J. Heat Transfer **135**, 021701 (2013).

[19] D. Maynes and J. Crockett, Apparent temperature jump and thermal transport in channels with streamwise rib and cavity featured superhydrophobic walls at constant heat flux, J. Heat Transfer **136**, 011701 (2014).

[20] D. Maynes, B. Webb, and J. Davies, Thermal transport in a microchannel exhibiting ultrahydrophobic microribs maintained at constant temperature, J. Heat Transfer **130**, 022402 (2008).

[21] A. Cowley, D. Maynes, and J. Crockett, Effective temperature jump and influence of axial conduction for thermal transport through channels with superhydrophobic walls, Int. J. Heat Mass Transf. **79**, 573 (2014).

[22] D. Maynes, M. Johnson, and B. W. Webb, Free-surface liquid jet impingement on rib patterned superhydrophobic surfaces, Phys. Fluids **23**, 052104 (2011).

[23] N. A. Patankar, Transition between superhydrophobic states on rough surfaces, Langmuir **20**, 7097 (2004).

[24] M. Reyssat, J. M. Yeomans, and D. Quéré, Impalement of fakir drops, Europhys. Lett. **81**, 26006 (2008).

[25] A. Lafuma and D. Quéré, Superhydrophobic states, Nat. Mater. **2**, 457 (2003).

[26] T. N. Krupenkin, J. A. Taylor, E. N. Wang, P. Kolodner, M. Hodes, and T. R. Salamon, Reversible wetting and dewetting transitions on electrically tunable superhydrophobic nanostructured surfaces, Langmuir **23**, 9128 (2007).

[27] D. Bartolo, F. Bouamrirene, É. Verneuil, A. Buguin, P. Silberzan, and S. Moulinet, Bouncing or sticky droplets: Impalement transitions on superhydrophobic micropatterned surfaces, Europhys. Lett. **74**, 299 (2006).

[28] G. Manukyan, J. M. Oh, D. van den Ende, R. G. H. Lammertink, and F. Mugele, Electrical Switching of Wetting States on Superhydrophobic Surfaces: A Route Towards Reversible Cassie-to-Wenzel Transitions, Phys. Rev. Lett. **106**, 014501 (2011).

[29] A. Dupuis and J. M. Yeomans, Modeling droplets on superhydrophobic surfaces? Equilibrium states and transitions, Langmuir **21**, 2624 (2005).

[30] T. Koishi, K. Yasuoka, S. Fujikawa, T. Ebisuzaki, and X. C. Zeng, Coexistence and transition between Cassie and Wenzel state on pillared hydrophobic surface, Proc. Natl. Acad. Sci. USA **106**, 8435 (2009).

[31] Q.-S. Zheng, Y. Yu, and Z.-H. Zhao, Effects of hydraulic pressure on the stability and transition of wetting modes of superhydrophobic surfaces, Langmuir **21**, 12207 (2005).

[32] B. He, N. A. Patankar, and J. Lee, Multiple equilibrium droplet shapes and design criterion for rough hydrophobic surfaces, Langmuir **19**, 4999 (2003).

[33] N. A. Patankar, On the modeling of hydrophobic contact angles on rough surfaces, Langmuir **19**, 1249 (2003).

[34] J. Bico, U. Thiele, and D. Quéré, Wetting of textured surfaces, Colloids Surf. A **206**, 41 (2002).

[35] M. Reyssat, A. Pepin, F. Marty, Y. Chen, and D. Quéré, Bouncing transitions on microtextured materials, Europhys. Lett. **74**, 306 (2006).

[36] Y. C. Jung and B. Bhushan, Dynamic effects induced transition of droplets on biomimetic superhydrophobic surfaces, Langmuir **25**, 9208 (2009).

[37] T. Deng, K. K. Varanasi, M. Hsu, N. Bhate, C. Keimel, J. Stein, and M. Blohm, Nonwetting of impinging droplets on textured surfaces, Appl. Phys. Lett. **94**, 133109 (2009).

[38] C. E. Clavijo, J. Crockett, and D. Maynes, Effects of isotropic and anisotropic slip on droplet impingement on a superhydrophobic surface, Phys. Fluids **27**, 122104 (2015).

[39] G. Rosengarten, A. Tetuko, K. Li, A. Wu, and R. Lamb, The effect of nano-strucutred surfaces on droplet impingement heat transfer, in *Proceedings of the ASME 2011 International Mechanical Engineering Congress and Exposition, Washington, DC* (ASME, New York, 2012).

[40] T. N. Krupenkin, J. A. Taylor, T. M. Schneider, and S. Yang, From rolling ball to complete wetting? The dynamic tuning of liquids on nanostructured surfaces, Langmuir **20**, 3824 (2004).

[41] T. Krupenkin, J. Taylor, P. Kolodner, and M. Hodes, Electrically tunable superhydrophobic nanostructured surfaces, Bell Labs Tech. J. **10**, 161 (2005).

[42] G. Liu, L. Fu, A. V. Rode, and V. S. J. Craig, Water droplet motion control on superhydrophobic surfaces: Exploiting the Wenzel-to-Cassie transition, Langmuir **27**, 2595 (2011).

[43] Z. Cheng, H. Lai, N. Zhang, K. Sun, and L. Jiang, Magnetically induced reversible transition between Cassie and Wenzel states of superparamagnetic microdroplets on highly hydrophobic silicon surface, J. Phys. Chem. C **116**, 18796 (2012).

[44] C. Lee and C.-J. Kim, Underwater Restoration and Retention of Gases on Superhydrophobic Surfaces for Drag Reduction, Phys. Rev. Lett. **106**, 014502 (2011).

[45] C. Stamatopoulos, T. M. Schutzius, C. J. Koppl, N. E. Hayek, T. Maitra, J. Hemrle, and D. Poulikakos, On the shedding of impaled droplets: The role of transient intervening layers, Sci. Rep. **6**, 18875 (2016).

[46] J. H. Snoeijer and B. Andreotti, Moving contact lines: Scales, regimes, and dynamical transitions, Annu. Rev. Fluid Mech. **45**, 269 (2013).

[47] Y. Liu, L. Moevius, X. Xu, T. Qian, J. Yeomans, and Z. Wang, Pancake bouncing on superhydrophobic surfaces, Nat. Phys. **10**, 515 (2014).

[48] C. Lee, Y. Nam, H. Lastakowski, J. I. Hur, S. Shin, A.-L. Biance, C. Pirat, C.-J. C. Kim, and C. Ybert, Two types of Cassie-to-Wenzel wetting transitions on superhydrophobic surfaces during drop impact, Soft Matter **11**, 4592 (2015).

[49] F. Incropera, D. DeWitt, T. Bergmann, and A. Lavine, *Fundamentals of Heat and Mass Transfer*, 6th ed. (John Wiley and Sons, New York, 2007).

[50] Y. C. Jung and B. Bhushan, Dynamic effects of bouncing water droplets on superhydrophobic surfaces, Langmuir **24**, 6262 (2008).

[51] N. Srivastava, C. Ding, A. Judson, N. MacDonald, and C. Meinhart, A unified scaling model for flow through a lattice of microfabricated posts, Lab Chip **10**, 1148 (2010).

[52] C. Ishino, M. Reyssat, E. Reyssat, K. Okumura, and D. Quere, Wicking within forests of micropillars, Europhys. Lett. **79**, 56005 (2007).

[53] P. G. de Gennes, Wetting: Statics and dynamics, Rev. Mod. Phys. **57**, 827 (1985).

[54] R. W. Fox, A. T. McDonald, and P. J. Pritchard, *Introduction to Fluid Mechanics*, 6th ed. (John Wiley and Sons, New York, 2004).

[55] S. Glasstone, K. Laidler, and H. Eyring, *The Theory of Rate Processes* (McGraw-Hill, New York, 1941).

[56] T. Blake, *Wettability* (Marcel Dekker, New York, 1993), Chap. 5.

[57] T. Blake and J. D. Coninck, The influence of solid-liquid interactions on dynamic wetting, Adv. Colloid Interface Sci. **96**, 21 (2002).

[58] M. J. de Ruijter, J. De Coninck, and G. Oshanin, Droplet spreading: Partial wetting regime revisited, Langmuir **15**, 2209 (1999).

[59] T. D. Blake, The physics of moving wetting lines, J. Colloid Interface Sci. **299**, 1 (2006).

[60] D. Duvivier, D. Seveno, R. Rioboo, T. D. Blake, and J. D. Coninck, Experimental evidence of the role of viscosity in the molecular kinetic theory of dynamic wetting, Langmuir **27**, 13015 (2011).